Magnetic quantum ratchet effect in Si-MOSFETs

S. D. Ganichev,[1] S. A. Tarasenko,[2] J. Karch,[1] J. Kamann,[1] and Z. D. Kvon[3]
[1] *Terahertz Center, University of Regensburg, 93040 Regensburg, Germany*
[2] *Ioffe Physical-Technical Institute, Russian Academy of Sciences, 194021 St. Petersburg, Russia and*
[3] *Institute of Semiconductor Physics, Russian Academy of Sciences, 630090 Novosibirsk, Russia*
(Dated: March 7, 2014)

We report on the observation of magnetic quantum ratchet effect in metal-oxide-semiconductor field-effect-transistors on silicon surface (Si-MOSFETs). We show that the excitation of an unbiased transistor by ac electric field of terahertz radiation at normal incidence leads to a direct electric current between the source and drain contacts if the transistor is subjected to an in-plane magnetic field. The current rises linearly with the magnetic field strength and quadratically with the ac electric field amplitude. It depends on the polarization state of the ac field and can be induced by both linearly and circularly polarized radiation. We present the quasi-classical and quantum theories of the observed effect and show that the current originates from the Lorentz force acting upon carriers in asymmetric inversion channels of the transistors.

PACS numbers: 72.40.+w, 78.40.Fy, 73.40.Qv, 78.20.-e

I. INTRODUCTION

A direct flow of charge carriers in semiconductor structures can be induced by *ac* electric force with zero average driving. Such phenomenon, referred to as the electronic ratchet effect [1], has been attracting much attention stimulated by both fundamental and applied interest in high-frequency non-linear electron transport at nanoscale [2–13]. By its origin, the ratchet transport can occur only in structures with space inversion asymmetry and, therefore, it provides a powerful tool to study the symmetry properties of nanostructures, anisotropy of the band structure, electron-phonon and electron-impurity interactions and etc. Intrinsic and extrinsic ratchet mechanisms can awake the additional carrier degrees of freedom and drive spin [14, 15] and valley [16, 17] currents. The application of an external static magnetic field breaks the time inversion symmetry giving rise to new mechanisms of current formation. In particular, it enables the magnetic quantum ratchet effect recently demonstrated for graphene layers excited by electromagnetic wave of terahertz (THz) range [18]. The effect emerges due to the joint orbital action of the *ac* electric and static magnetic fields on two-dimensional (2D) electron gas in systems with structure inversion asymmetry (SIA). The latter leads to an asymmetric scattering of carriers in the momentum space resulting in a direct electric current [19, 20]. While the SIA in graphene results from indistinct factors, such as adatoms on its surface, it be obtained in a controllable way by application of a gate voltage to the electron channel in field-effect transistors. Consequently, studying the magnetic quantum ratchet in such systems provides an access to the better understanding of this phenomenon.

Here, we report the observation and study of the magnetic quantum ratchet transport of electrons in Si-based field-effect-transistors (MOSFETs). We show that the excitation of the electron gas in the inversion channel of Si-MOSFETs subjected to an in-plane magnetic field by *ac* electric field, here of THz radiation, leads to a direct electric current between the unbiased source and drain contacts. The current is proportional to the square of the ac electric field amplitude, scales linearly with the magnetic field strength, and reverses its direction by switching the magnetic field polarity. It can be generated by both linearly polarized and circularly polarized radiation. For linear polarization, the current depends on the angle between the electric field polarization and the static magnetic field. For circular polarization, the current reveals a helicity-sensitive component reversing its sign by switching the rotation direction of the electric field. We present the microscopic model of the effect as well as the quasi-classical and quantum theories explaining all major features observed in experiment. It is shown that the action of the Lorentz force on the electron motion induced by high-frequency electric field affects the electron scattering yielding an asymmetric distribution of nonequilibrium electrons.

II. SAMPLES AND TECHNIQUE

We study n-type MOSFETs fabricated on (001)-oriented silicon surfaces by means of standard metal-oxide-semiconductor technology including preparation of SiO_2 with a thickness of 110 nm by high temperature oxidation of silicon, preparation of heavily doped n^{++} contacts by ion-implantation, and the fabrication of heavily doped polycrystalline semitransparent gates. Transistor with a channel length of 3 mm and a width of 2.8 mm were prepared along $y \parallel [110]$. A doping level N_a of the depletion layer was of about $3 \times 10^{15}\,\mathrm{cm}^{-3}$. In these transistors, the variation of the gate voltage V_g from 1 to 20 V changes the carrier density N_s from about 1.9×10^{11} to $3.8 \times 10^{12}\,\mathrm{cm}^{-2}$ and the energy spacing ε_{21} between the size-quantized subbands $e1$ and $e2$ from 10 to 35 meV [21]. Dependence of the election mobility μ on the electron density obtained by electrical measure-

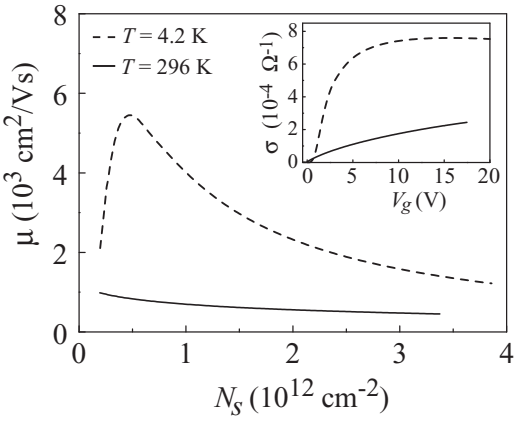

FIG. 1: Dependence of mobility on electron density for the samples studied at room and liquid helium temperature. Inset shows the gate voltage dependence of the channel conductivity.

ments in the samples under study at room and liquid helium temperatures is shown in Fig. 1. The dependence is standard for Si-MOSFETs: at room temperature the mobility is close to that in bulk Si at low electron density and then smoothly decreases with the increase of N_s due to the enhancement of electron-phonon scattering. At $T = 4.2$ K, the mobility is a non-monotonic function of the electron density, which is caused by interplay of electron scattering by impurities in Si and roughness at Si-SiO_2 interface [21]. The peak mobilities μ at room and liquid helium temperature are approximately 700 and 6×10^3 cm^2/Vs, respectively.

To generate ratchet currents in unbiased samples we used alternating electric fields $\boldsymbol{E}(t)$ of a pulsed terahertz NH_3 laser, optically pumped by a transversely excited atmosphere pressure (TEA) CO_2 laser [22, 23]. The laser operated at frequencies $f = 3.32$ THz (wavelength $\lambda = 90.5$ μm), 2.03 THz ($\lambda = 148$ μm) or 1.07 THz ($\lambda = 280$ μm). It provides single pulses with a duration of about 100 ns, peak power of $P \approx 30$ kW, and a repetition rate of 1 Hz. The radiation power was controlled by the THz photon drag detector [24]. The radiation at normal incidence was focused in a spot of about 1 to 3 mm diameter. The spatial beam distribution had an almost Gaussian profile which was measured by a pyroelectric camera [25]. The experimental geometry is illustrated in Fig. 2. All experiments are performed at room temperature and normal incidence of radiation. In this geometry, the THz radiation causes *intra*subband indirect optical transitions (Drude-like free carrier absorption). An external in-plane magnetic field $\boldsymbol{B}$ of ± 1 T was applied, either perpendicular or parallel to the MOSFET channel, see Fig. 2. The photocurrents are measured between the source and drain contacts of the unbiased transistors via the voltage drop across a 50 Ω load resistor.

To vary the radiation polarization, $\lambda/2$ and $\lambda/4$ crystal quartz plates were employed. By applying the $\lambda/2$ plates, we varied the azimuth angle α between the polarization

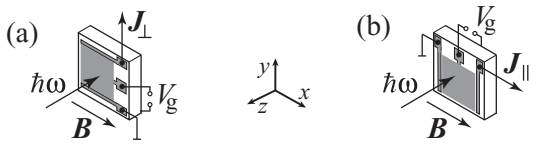

FIG. 2: Experimental configurations. The photocurrent components are measured in the (a) transverse and (b) longitudinal geometry with respect to the static magnetic field $\boldsymbol{B}$.

plane of the radiation incident upon the sample and the y axis. By applying $\lambda/4$ plates, we obtained elliptically (and circularly) polarized radiation. In this case, the polarization state is determined by the angle φ between the plate optical axis and the incoming laser polarization with electric field vector along the y axis. In particular, the radiation helicity is given by $P_{\rm circ} = \sin 2\varphi$ [26]. The incident polarization states are sketched for characteristic angles φ on top of Fig. 4.

III. EXPERIMENTAL RESULTS

Irradiating the transistors with polarized THz radiation we observed a dc electric response, which scales linearly with the magnetic field strength and changes its sign by reversing the magnetic field direction, see inset in Fig. 3. For zero magnetic field the current vanishes. The measured electric current pulses are of about 100 ns duration and reflect the corresponding laser pulses. The photocurrent is detected in the direction perpendicular to the magnetic field (transverse photocurrent, Fig. 2a) as well as along $\boldsymbol{B}$ (longitudinal photocurrent, Fig. 2b). These photocurrents exhibit characteristic polarization dependences which are different for linear and elliptical polarized radiation.

Figure 3 shows the dependence of the transverse and longitudinal photocurrents on the *ac* electric field azimuth angle α obtained for sample 1. The experimental data can be well fitted by

$$J_\perp(\alpha) = \chi_1 \cos 2\alpha + \chi_2\,, \quad J_\parallel(\alpha) = \chi_1 \sin 2\alpha, \qquad (1)$$

where χ_1 and χ_2 are fit parameters, see solid fit curves in Fig. 3. Figure 3 and Eqs. (1) reveal that the polarization dependent contributions to the transverse and longitudinal photocurrents vary according to the Stokes parameters of THz radiation $S_1 = \cos 2\alpha$ and $S_2 = \sin 2\alpha$ multiplied by the same fit coefficient χ_1. The polarization independent contribution is detected for the transverse photocurrent only and is described by the parameter χ_2.

The photocurrent in response to elliptically polarized radiation is shown in Fig. 4. In this case, the transverse and longitudinal photocurrent components can be well fitted by

$$J_\perp = \chi_1 \cos^2 2\varphi + \chi_2\,, \quad J_\parallel = \frac{\chi_1}{2} \sin 4\varphi + \chi_3 P_{\rm circ}\,. \qquad (2)$$

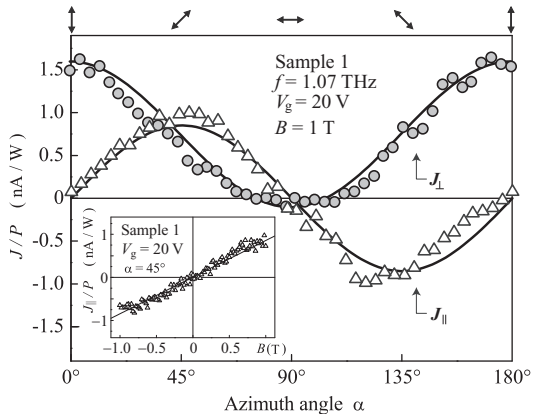

FIG. 3: Photocurrent as a function of the azimuth angle α measured in sample 1 in the direction perpendicular and parallel to the magnetic field. The data are obtained for the gate voltage $V_g = 20$ V and radiation frequency $f = 1.07$ THz. Lines are fits to Eqs. (1). The inset shows the behavior of the longitudinal photocurrent $J_\parallel$ upon variation of the magnetic field strength. The arrows on top illustrate the polarization states for different angles α.

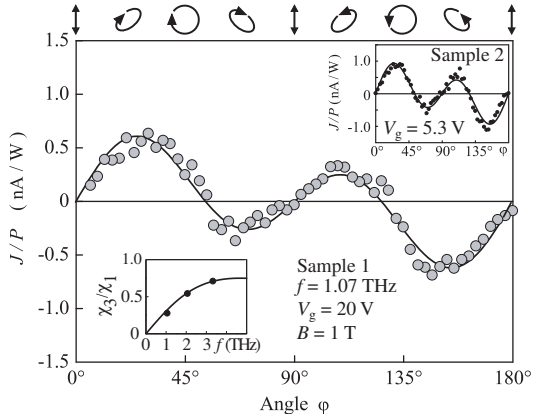

FIG. 4: Photocurrent as a function of the radiation helicity measured in the direction parallel to the magnetic field. The data are obtained for sample 1 at the gate voltage $V_g = 20$ V and the radiation frequency $f = 1.07$ THz. The right inset shows the polarization dependence of the photocurrent measured in the same geometry for sample 2 at $V_g = 5.3$ V. The lines are a fit to the phenomenological Eq. (2). The left inset presents the behavior of the ratio of magnetic field induced circular and linear photocurrents upon variation of the wavelength. On top, the polarization ellipses corresponding to various angles φ are illustrated.

Obviously all current contributions measured for linearly polarized radiation are detected in the experimental geometry applying a $\lambda/4$-plate. These are the terms proportional to the fit parameters χ_1 and χ_2. The only change is the functional behavior of the Stokes parameters which now are given by $S_1 = \cos^2 2\varphi$ and $S_2 = \sin 4\varphi/2$. In the longitudinal geometry, however, a new photocurrent contribution is observed. It is proportional to the radiation helicity $P_{\rm circ}$ corresponding to the third

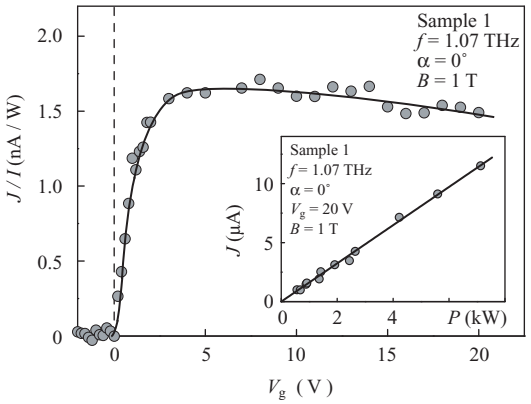

FIG. 5: Gate dependence of the transverse photocurrent. Solid curve is a guide for eye. Inset shows its intensity dependence measured at $V_g = 20$ V.

Stokes parameter S_3. This contribution exhibits the sign inversion upon switching the radiation helicity $P_{\rm circ}$ from +1 to -1 at $\varphi = 45°$ (σ_+) and $\varphi = 135°$ (σ_+), respectively. We note that, for pure circularly polarized radiation, the Stokes parameters S_1 and S_2 vanish. Similar to the photocurrent induced by linearly polarized radiation, the circular photocurrent linearly scales with the magnetic field strength (not shown).

Applying the radiation of various frequencies, we observed that the ratio χ_3/χ_1, which determines the relative magnitude of the circular and linear photocurrents, increases with raising the radiation frequency f at small f. The corresponding spectral dependence of χ_3/χ_1 is shown in the left inset in Fig. 4.

The dependence of photocurrent on the gate voltage V_g is presented in Fig. 5. At negative V_g, the photoresponse is absent since no inversion channel is formed on the silicon surface. At positive gate voltage, the photocurrent linearly increases with V_g at small voltages, reaches a maximum, and then slowly decreases with the further increase of V_g. For the whole range of gate voltages, the photocurrent is proportional to the radiation intensity, i.e., the squared amplitude of the radiation electric field. An example of the measured intensity dependence of the photocurrent is shown in the inset in Fig. 5.

Now we discuss the microscopic mechanism of the dc current generation. Generally, the current can arise due to an intrinsic asymmetry of electron transport in the inversion channel driven by ac electric field [16, 27] or macroscopic in-plane asymmetry of the transistor structure, e.g., due to illumination of occasionally unequal contacts [28–30]. The fact that the current vanishes in the absence of the static magnetic field rules out the macroscopic in-plane asymmetry of the transistor structure as a source of the current formation. At the same time, all the observations, including linear dependence of the dc electric current on the static magnetic field, square dependence of the current on the radiation field amplitude as well as the polarization behavior, exhibit

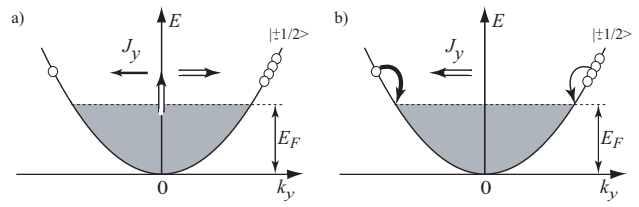

FIG. 6: Orbital mechanisms underlying the generation of the MPGE current. (a) Excitation and (b) relaxation mechanisms.

the recognized behavior of the magnetic quantum ratchet effect [18].

IV. MICROSCOPIC THEORY

Microscopic mechanisms responsible for the observed ratchet effect in Si-based structures involve asymmetry of the photoexcitation (excitation mechanism) or relaxation (relaxation mechanism). Both mechanisms are of a pure orbital origin and based on the asymmetry of electron scattering by static defects or phonons in the momentum space [19, 31, 32]. The scattering asymmetry is caused by the Lorentz force acting upon carriers in inversion channels. It is describe by the correction to the scattering rate $W_{\boldsymbol{k}'\boldsymbol{k}}$ that is linear in the wave vector and in-plane magnetic field. Such a correction is allowed in gyrotropic structures only and, in Si-MOSFETs, is caused by structure inversion asymmetry of inversion channels. It can be obtained microscopically by considering the magnetic field induced change of the electron wave function, which yields [32]

$$W_{\boldsymbol{k}'\boldsymbol{k}} = W^{(0)}_{\boldsymbol{k}'\boldsymbol{k}} + w[B_x(k_y + k'_y) - B_y(k_x + k'_x)] \,, \quad (3)$$

where $\boldsymbol{k}$ and $\boldsymbol{k}'$ are the initial and scattered wave vectors, $W^{(0)}_{\boldsymbol{k}'\boldsymbol{k}}$ is the scattering rate at $\boldsymbol{B} = 0$, and the coefficient w describes the scattering asymmetry degree. Due to linear in the wave vector terms in $W_{\boldsymbol{k}'\boldsymbol{k}}$, the scattering processes to the states $\boldsymbol{k}'$ and $-\boldsymbol{k}'$ occur at different probabilities, which results in asymmetric distribution of electrons in $\boldsymbol{k}$-space if the electron gas is driven out of equilibrium. This is the origin of *dc* electric current in Si-MOSFETs excited by terahertz radiation.

The excitation and relaxation mechanisms of the current generation are illustrated in Figs. 6 (a) and (b), respectively. Figure 6 (a) sketches the intrasubband absorption of radiation (Drude absorption) which includes a momentum transfer from phonons or impurities to electrons to satisfy momentum conservation. The vertical arrow shows electron-photon interaction while the horizontal arrows describe the elastic scattering events to the final state with either positive or negative electron wave vector k'_x. In the in-plane magnetic field, the probabilities of scattering to positive and negative k'_x are not equal, which is shown by the horizontal arrows of different thickness. This leads to an asymmetric distribution of photoexcited carriers in $\boldsymbol{k}$-space, i.e., an electric current $\boldsymbol{j}$. For simplicity, we have drawn transitions only from the initial state $k_x = 0$, however the argument holds for arbitrary k_x as well. The electric current $\boldsymbol{j}$ is odd in the magnetic field $\boldsymbol{B}$ because the asymmetric part of scattering rate is proportional to $\boldsymbol{B}$, see Eq. (3), and the probabilities for scattering to the positive or negative k'_x are inverted for the fields $\boldsymbol{B}$ and $-\boldsymbol{B}$. For linearly polarized radiation, the momenta of photoexcited carriers are preferably aligned along the electric field of radiation. Therefore, for a fixed magnetic field, the current direction and magnitude depend on the radiation polarization state. The electric current caused by asymmetry of photoexcitation decays within the typical momentum relaxation time of electrons after the irradiation is switched off.

Similarly to photoexcitation, the energy relaxation of hot carriers due to inelastic scattering by phonons is also asymmetric in $\boldsymbol{k}$-space, which leads to an additional contribution to the electric current. This relaxation mechanism is illustrated in Fig. 6 (b) where the curved arrows of different thickness show the inequality of relaxation rates at positive and negative k_x. The relaxation photocurrent is also odd in the magnetic field $\boldsymbol{B}$. However, it is independent of the radiation polarization and decays within the energy relaxation time after the optical excitation pulse. Thus, photocurrent measurements with high time resolution can be used to distinguish between the excitation and relaxation mechanisms.

Below, we present quasi-classical and quantum theories of magnetic quantum ratchet effect. The quasi-classical approach is valid provided the photon energy $\hbar\omega$ is much smaller than the mean kinetic energy of carriers $\tilde{\varepsilon}$ and developed in the framework of Boltzmann's equation. The quantum theory is required if $\hbar\omega$ is comparable to or exceeds $\tilde{\varepsilon}$ and involves the quantum mechanical consideration of intrasubband optical transitions. For simplicity, we consider below the carriers in the ground subband of size quantization $e1$. The population of excited subbands at high temperature or small gate voltage may modify the current amplitude.

A. Quasi-classical approach

The quasi-classical theory of the magnetic quantum ratchet effect is developed following Refs. [19, 20]. In this approach, the electric field of the radiation $\boldsymbol{E}(t) = \boldsymbol{E}\exp(-i\omega t) + \boldsymbol{E}^*\exp(i\omega t)$ is considered as *ac* force acting upon charge carriers. The electron distribution function $f_{\boldsymbol{k}}$ in $\boldsymbol{k}$-space is found from the Boltzmann equation

$$\frac{\partial f_{\boldsymbol{k}}}{\partial t} + e\boldsymbol{E}(t)\cdot\frac{\partial f_{\boldsymbol{k}}}{\hbar\,\partial \boldsymbol{k}} = \mathrm{St} f_{\boldsymbol{k}} \,, \quad (4)$$

where $\mathrm{St} f_{\boldsymbol{k}}$ is the collision integral. For elastic scattering, $\mathrm{St} f_{\boldsymbol{k}}$ has the form

$$\mathrm{St} f_{\boldsymbol{k}} = \sum_{\boldsymbol{k}'} (W_{\boldsymbol{k}\boldsymbol{k}'} f_{\boldsymbol{k}'} - W_{\boldsymbol{k}'\boldsymbol{k}} f_{\boldsymbol{k}'}) \,, \quad (5)$$

where $W_{\boldsymbol{k}'\boldsymbol{k}}$ is the scattering rate. Taking into account the admixture of excited-subband states to the ground-subband wave function in the in-plane magnetic field $\boldsymbol{B}$, one obtains the matrix element of electron scattering [32]

$$V_{\boldsymbol{k}'\boldsymbol{k}} = V_{11} - \frac{e\hbar[B_x(k_y+k'_y) - B_y(k_x+k'_x)]}{m^*c} \sum_{\nu\neq 1} \frac{z_{\nu 1} V_{1\nu}}{\varepsilon_{\nu 1}} \tag{6}$$

and the scattering rate Eq. (3) with the parameters

$$W^{(0)}_{\boldsymbol{k}'\boldsymbol{k}} = \frac{2\pi}{\hbar} |V_{11}|^2 \, \delta(\varepsilon_{\boldsymbol{k}} - \varepsilon_{\boldsymbol{k}'}) \, , \tag{7}$$

$$w = -\frac{4\pi e}{m^*c} \sum_{\nu\neq 1} \frac{z_{\nu 1}}{\varepsilon_{\nu 1}} \, \mathrm{Re}(V^*_{11} V_{1\nu}) \, \delta(\varepsilon_{\boldsymbol{k}} - \varepsilon_{\boldsymbol{k}'}) \, . \tag{8}$$

Here, V_{11} and $V_{1\nu}$ ($\nu \neq 1$) are the matrix elements of intrasubband and intersubband scattering at $\boldsymbol{B} = 0$, ν is the subband index, $\varepsilon_{\boldsymbol{k}} = \hbar^2\boldsymbol{k}^2/(2m^*)$, m^* is the effective mass in the channel plane, e is the electron charge, $z_{\nu 1}$ are the coordinate matrix elements, and $\varepsilon_{\nu 1}$ are the energy distances between the subbands. Note that, for Si-MOSFETs on the (001) surface, the in-plane mass m^* is given by $m_\perp$ while the energies $\varepsilon_{\nu 1}$ are determined by $m_\parallel$, where $m_\perp$ and $m_\parallel$ are the transversal and longitudinal effective electron mass in bulk Si.

The electric current density is given by

$$\boldsymbol{j} = 4e \sum_{\boldsymbol{k}} \boldsymbol{v}_{\boldsymbol{k}} f_{\boldsymbol{k}} \, , \tag{9}$$

where $\boldsymbol{v}_{\boldsymbol{k}} = \hbar\boldsymbol{k}/m^*$ is the velocity and the factor 4 accounts for the spin and valley degeneracy. By solving the Boltzmann equation (4) to second order in the electric field amplitude $\boldsymbol{E}$ and first order in the static magnetic field $\boldsymbol{B}$ one obtains *dc* electric current. Calculation shows that the y component of the current is given by

$$j_y = (M_1 S_1 - M_2)|\boldsymbol{E}|^2 B_x + (M_1 S_2 + M_3 S_3)|\boldsymbol{E}|^2 B_y, \tag{10}$$

where $S_1 = (|E_x|^2 - |E_y|^2)/|\boldsymbol{E}|^2$, $S_2 = (E_x E_y^* + E_y E_x^*)/|\boldsymbol{E}|^2$, and $S_3 = \mathrm{i}(E_x E_y^* - E_y E_x^*)/|\boldsymbol{E}|^2$ are the Stokes parameters determined by the radiation polarization,

$$M_1 = \frac{\zeta \, e^4}{\pi m^* c\hbar^2} \int_0^\infty \frac{\tau_1 \, (\tau_1\tau_2 \, \varepsilon^2)' f'_0 \, d\varepsilon}{1 + (\omega\tau_1)^2} \, , \tag{11}$$

$$M_2 = \frac{\zeta \, e^4}{\pi m^* c\hbar^2} \int_0^\infty \frac{(1 - \omega^2\tau_1\tau_2)\tau_1\tau_2 \, \varepsilon^2 \tau'_1 f'_0 \, d\varepsilon}{[1 + (\omega\tau_1)^2][1 + (\omega\tau_2)^2]} \, , \tag{12}$$

$$M_3 = -\frac{\zeta \, e^4}{\pi m^* c\hbar^2} \int_0^\infty \frac{\omega\tau_1\tau_2(\tau_1 + \tau_2) \, \varepsilon^2 \tau'_1 f'_0 \, d\varepsilon}{[1 + (\omega\tau_1)^2][1 + (\omega\tau_2)^2]} \, , \tag{13}$$

$\zeta = (4m^*/\hbar^3) \sum_{\nu\neq 1} z_{\nu 1} \mathrm{Re}(\mathrm{V}^*_{11}\mathrm{V}_{1\nu})/\varepsilon_{\nu 1}$, τ_1 and τ_2 are respectively the relaxation times of the first and second angular harmonics of the distribution function in the absence of magnetic field,

$$\tau_n^{-1} = \sum_{\boldsymbol{k}'} W^{(0)}_{\boldsymbol{k}\boldsymbol{k}'} (1 - \cos n\theta_{\boldsymbol{k}'\boldsymbol{k}}) \, ,$$

$\theta_{\boldsymbol{k}'\boldsymbol{k}}$ is the angle between the wave vectors $\boldsymbol{k}'$ and $\boldsymbol{k}$, $\tau'_1 = d\tau_1/d\varepsilon$, $f'_0 = df_0(\varepsilon)/d\varepsilon$, and $f_0(\varepsilon)$ is the function of equilibrium carrier distribution.

Equations (10)-(13) describe the excitation mechanism of current formation. The first and second terms on the right-hand side of Eq. (10) stand for the current components perpendicular and parallel to the applied magnetic field, respectively. The perpendicular component contains the contribution sensitive to linear polarization of the radiation, $\propto S_1$, and the polarization independent term. The parallel component depends on both linear, $\propto S_2$, and circular, $\propto S_3$, polarization states of the radiation.

At small frequencies of the ac electric field, the linear photocurrent given by M_1 is independent of ω while the circular photocurrent given by M_3 is proportional to ω, as observed in the experiment. Considering the Boltzmann distribution of carriers, $f_0(\varepsilon) \propto \exp(-\varepsilon/k_BT)$, and the power dependence of the relaxation times on energy, $\tau_1(\varepsilon) = a\varepsilon^r$, $\tau_2(\varepsilon)/\tau_1(\varepsilon) = (2-r)/2$, one obtains

$$\frac{M_3}{M_1} = \omega\tau_1(k_BT) \frac{r(r-4)}{4(r+1)} \frac{\Gamma(4r+2)}{\Gamma(3r+2)} \, , \tag{14}$$

where $\Gamma(x)$ is the Gamma function. At high frequency, $\omega \gg 1/\tau_1$, the linear and circular currents decrease as $1/\omega^2$ and $1/\omega^3$, respectively, and the linear current dominates.

We note that that the energy relaxation of hot carriers in the in-plane magnetic field leads to an additional contribution to the polarization-independent current given by M_2, see Fig. 6(b). This contribution depends on the details of electron-phonon scattering and was theoretically addressed in Refs. [31, 32].

B. Quantum approach

The relevant description of the magnetic ratchet effect in the quantum regime involves the consideration of indirect intrasubband optical transitions. Due to energy and momentum conservation, the intrasubband absorption of radiation is accompanied by electron scattering from static defects or phonons. Such second-order processes are theoretically described by virtual transitions with intermediate states. Taking into account the virtual transitions via states in the ground and excited electron subbands one can obtain the matrix element of the intrasubband transitions $\boldsymbol{k} \to \boldsymbol{k}'$. To first order in the in-plane magnetic field, the matrix element of the intrasubband transitions accompanied by elastic electron scattering has

the form

$$M_{\boldsymbol{k}'\boldsymbol{k}} = \frac{e\boldsymbol{A}\cdot(\boldsymbol{k}'-\boldsymbol{k})}{c\,\omega\,m^*}V_{\boldsymbol{k}'\boldsymbol{k}} - 2\frac{e^2(A_xB_y - A_yB_x)}{m^*c^2}\sum_{\nu\neq 1}\frac{z_{\nu 1}}{\varepsilon_{\nu 1}}V_{1\nu}, \tag{15}$$

where $\boldsymbol{A}$ is the amplitude of the electromagnetic field vector potential, $\boldsymbol{A} = (-ic/\omega)\boldsymbol{E}$.

The radiation absorption in the presence of the in-plane magnetic field leads to an asymmetry in the electron distribution in $\boldsymbol{k}$-space and, hence, to an electric current. The anisotropic part of the electron distribution function can be found from the master equation

$$g_{\boldsymbol{k}} = \mathrm{St} f_{\boldsymbol{k}}\,, \tag{16}$$

where $g_{\boldsymbol{k}}$ is the generation rate due to intrasubband optical transitions

$$g_{\boldsymbol{k}} = \frac{2\pi}{\hbar}\sum_{\boldsymbol{k}',\pm}|M_{\boldsymbol{k}'\boldsymbol{k}}|^2[f_0(\varepsilon_{\boldsymbol{k}'}) - f_0(\varepsilon_{\boldsymbol{k}})]\,\delta(\varepsilon_{\boldsymbol{k}'} - \varepsilon_{\boldsymbol{k}} \pm \hbar\omega). \tag{17}$$

Taking into account linear-in-$\boldsymbol{B}$ terms both in the generation rate $g_{\boldsymbol{k}}$ and the collision integral $\mathrm{St} f_{\boldsymbol{k}}$ one can calculate the asymmetric part of the distribution function and the electric current. The electric current originating from the asymmetric part of $g_{\boldsymbol{k}}$ contains both polarization-dependent and polarization-independent contributions. It is caused by asymmetry of optical transitions in $\boldsymbol{k}$-space and decays with the momentum relaxation time. The current stemming from the asymmetric part of $\mathrm{St} f_{\boldsymbol{k}}$ is polarization-dependent and vanishes for unpolarized radiation. It can be interpreted in terms of the optical alignment of electron momenta in $\boldsymbol{k}$-space by linearly polarized radiation followed by scattering asymmetry. Generally, the current contributions originating from the asymmetry of the generation rate and the collision integral are comparable to each other. For a particular case of short-range scattering, where the relaxation times of all non-zero angular harmonics of the distribution function coincide and are independent of energy, the electric current is given by Eq. (10) with

$$M_1 = -\frac{\zeta\, e^4\,\tau_1}{\pi m^* c\hbar^3\omega^3}\int\limits_0^\infty (2\varepsilon + \hbar\omega)[f_0(\varepsilon) - f_0(\varepsilon + \hbar\omega)]d\varepsilon\,. \tag{18}$$

Equation (18) is valid for $\omega\tau_1 \gg 1$ and can be considered as an extension of Eq. (11) to high-frequency range. Naturally, both the quasi-classical and quantum approaches unite and yield the same result, compare Eqs. (11) and (18), for the intermediate frequency range $1/\tau_1 \ll \omega \ll \tilde{\varepsilon}/\hbar$.

C. Estimation for triangular channel

Before discussing experimental results in a view of the developed theory we estimate the ratchet current magnitude for Si-MOSFET structures. As follows from Eqs. (10) and (11) obtained within the quasi-classical approach, the polarization-dependent contribution to the current induced by linearly polarized radiation for $\omega\tau_1 \leq 1$ and short-range scattering is given by

$$j = \frac{4e^4\tau_1^2 N_s B E^2}{c\,m^{*2}}\left|\sum_{\nu\neq 1}\frac{z_{\nu 1}}{\varepsilon_{\nu 1}}\,\xi_\nu\right|\,, \tag{19}$$

where $\xi_\nu = \mathrm{Re}(\mathrm{V}_{11}^*\mathrm{V}_{1\nu})/|\mathrm{V}_{11}|^2$ and N_s is the electron density. We assume that electrons in Si-MOSFET are confined in the triangular channel with the potential energy $U(z) = \infty$ for $z < 0$ and $U(z) = |eF|z$ for $z > 0$, where F is the effective electric field. The electron wave functions and energies for the triangular channel have the form

$$\varphi_\nu(z) = C_\nu\left(\frac{2m_\parallel|eF|}{\hbar^2}\right)^{1/6}\mathrm{Ai}\left[\left(\frac{2m_\parallel|eF|}{\hbar^2}\right)^{1/3}z + \lambda_\nu\right]\,,$$

$$\varepsilon_\nu = -\left(\frac{\hbar^2|eF|^2}{2m_\parallel}\right)^{1/3}\lambda_\nu\,, \tag{20}$$

where C_ν are the normalization constants, $\mathrm{Ai}(z)$ is the Airy function, and $\lambda_\nu < 0$ are the roots of the Airy function. The coordinate matrix elements and the energy distances between the subbands are respectively given by

$$z_{\nu 1} = C_1C_\nu\left(\frac{\hbar^2}{2m_\parallel|eF|}\right)^{1/3}\int_0^\infty \mathrm{Ai}(x+\lambda_\nu)x\mathrm{Ai}(x+\lambda_1)dx\,, \tag{21}$$

$$\varepsilon_{\nu 1} = \left(\frac{\hbar^2|eF|^2}{2m_\parallel}\right)^{1/3}(\lambda_1 - \lambda_\nu)\,. \tag{22}$$

For the model of short-range scatterers uniformly distributed in the channel, which is also relevant for quasi-elastic electron scattering by acoustic phonons, the parameters ξ_ν have the form

$$\xi_\nu = \frac{\int\varphi_1^3(z)\varphi_\nu^3(z)dz}{\int\varphi_1^4(z)dz} = \frac{C_\nu}{C_1}\frac{\int\mathrm{Ai}^3(x+\lambda_1)\mathrm{Ai}(x+\lambda_\nu)dx}{\int\mathrm{Ai}^4(x+\lambda_1)dx}\,. \tag{23}$$

Therefore, we finally obtain

$$j = \frac{4e^4\tau_1^2 N_s B E^2}{c\,m^{*2}|eF|}|\mathcal{C}|\,, \tag{24}$$

where $\mathcal{C}$ is the dimensionless parameter,

$$C = \sum_{\nu\neq 1}\frac{C_\nu^2}{\lambda_1 - \lambda_\nu}\frac{\int_0^\infty \mathrm{Ai}^3(x+\lambda_1)\mathrm{Ai}(x+\lambda_\nu)dx}{\int_0^\infty \mathrm{Ai}^4(x+\lambda_1)dx} \times \int_0^\infty \mathrm{Ai}(x+\lambda_\nu)x\mathrm{Ai}(x+\lambda_1)dx \approx -0.085\,. \tag{25}$$

Note, that the amplitude E of the electric field acting upon the carriers in the sample is related to the laser radiation intensity I by $E = t\sqrt{2\pi I/c}$, where $t = 2/(n_\omega + 1)$ is the amplitude transmission coefficient for the normally incident radiation and n_ω is the refractive index.

V. DISCUSSION

The microscopic theory of the magnetic quantum ratchet effect presented above describes all major features observed in the experiment. First, it shows that the direct electric current is proportional to the square of the ac electric field amplitude $\boldsymbol{E}$, i.e., proportional to the radiation intensity I, scales linearly with the in-plane magnetic field $\boldsymbol{B}$ and reverses its direction by changing the magnetic field polarity, see Eq. (10). Such a behavior is observed in the experiment. Second, Eq. (10) demonstrates that the current components perpendicular to and along the static magnetic field has different polarization dependence: the perpendicular component contains the contribution determined by the Stokes parameter S_1 and polarization independent term while the parallel component depends on both linear, $\propto S_2$, and circular, $\propto S_3$, polarization states of the radiation. Exactly this polarization behavior of the photocurrent is observed in the experiment, see Figs. 3 and 4 and the empirical fit Eqs. (1) and (2). Third, according to Eqs. (14) the ratio of the linear to circular contributions to the ratchet current is proportional to the radiation frequency ω at $\omega\tau_1 < 1$, which also corresponds to the experimental data, see left inset in Fig. 4. Fourth, the theory explains the observed behavior of the current magnitude with the gate voltage change. Indeed, it follows from Eq. (24) that the gate voltage dependence of the ratchet current is theoretically given by $j(V_g) \propto \mu^2(V_g)N_s(V_g)/F(V_g)$. At small positive gate voltage, the current linearly scales with V_g which is caused by the linear dependence of the carrier density on V_g. At higher V_g, the current saturates and then exhibits a slow decrease with the further growth of V_g which is related to the decrease of mobility μ and increase of the effective electric field F. Finally, we estimate the ratchet current magnitude for Si-MOSFETs following Eq. (24). The estimation of the current density j normalized by the laser radiation intensity I yields $j/I \sim 1 \times 10^{-9}\,\mathrm{A\,cm/W}$ for the electron density $N_s = 3.8 \times 10^{12}\,\mathrm{cm}^{-2}$, relaxation time $\tau_1 = 0.5 \times 10^{-13}\,\mathrm{s}$ determined from the room-temperature mobility $400\,\mathrm{cm}^2/\mathrm{V\,s}$, the effective field $F = 1.4 \times 10^5\,\mathrm{V/cm}$ obtained from the energy distance $\varepsilon_{21} = 35\,\mathrm{meV}$ at $V_g = 20\,\mathrm{V}$ [21], magnetic field $B = 1\,\mathrm{T}$, the effective in-plane mass $m^* \approx 0.2m_0$ and the longitudinal mass in the valley $m_\parallel \approx 0.92m_0$, with m_0 being the free electron mass, and silicon refractive index of silicon $n_\omega \approx 3.4$. For the $3 \times 3\,\mathrm{mm}^2$ transistor and the similar laser beam cross section, it gives $J/P \sim 3 \times 10^{-9}\mathrm{A/W}$, which is close to the signal magnitude detected in the experiment, see Fig. 3. Thus, the simple model of the inversion channel with no fit parameters provides the quantitatively correct magnitude of the ratchet current.

VI. SUMMARY

To summarize, we have demonstrated the room-temperature magnetic quantum ratchet effect in Si-based metal-oxide-semiconductor field-effect-transistors with electron inversion channels. The direct current between the source and drain contacts of the unbiased transistor is excited by ac electric field with zero average driving in the presence of the static in-plane magnetic field. The effect is caused by orbital effects of the electric and field on two-dimensional electron gas confined in an asymmetric channel. It could be employed for designing the fast polarization-resolved Si-based detectors of terahertz and microwave radiation.

Acknowledgments

Support from DFG (SFB 689), Linkage Grant of IB of BMBF at DLR, RFBR, and RF President Grant MD-3098.2014.2 is gratefully acknowledged.

[1] Hänggi P and Marchesoni F 2009 *Rev. Mod. Phys.* **81** 387
[2] Linke H, Humphrey T E, Löfgren A, Sushkov A O, Newbury R, Taylor R P and Omling P 1999 *Science* **286**5448
[3] Entin M V and Magarill L I 2006 it Phys. Rev. B **73** 205206
[4] Sassine S, Krupko Yu, Portal J-C, Kvon Z D, Murali R, Martin K P, Hill G and Wieck A D 2008 *Phys. Rev. B* **78** 045431
[5] Smirnov S, Bercioux D, Grifoni M and Richter K 2008 *Phys. Rev. Lett.* **100** 230601
[6] Olbrich P, Ivchenko E L, Ravash R, Feil T, Danilov S D, Allerdings J, Weiss D, Schuh D, Wegscheider W and Ganichev S D *Phys. Rev. Lett* **103** 090603
[7] Brizhik L S, Eremko A A, Piette B M A G and Zakrzewski W J 2010 *J. Phys.: Condens. Matter* **22** 155105
[8] Miyamoto S, Nishiguchi K, Ono Yu, Itoh K M and Fujiwara A 2010 *Phys. Rev. B* **82** 033303
[9] Roeling E M, Germs W C, Smalbrugge B, Geluk E J, de Vries T, Janssen R A J and Kemerink M 2011 *Nature Mater.* **10** 51
[10] Chepelianskii A D, Entin M V, Magarill L I and Chepelyansky D L 2007 *Eur. Phys. J. B* **56** 323
[11] Popov V V 2013 *Appl. Phys. Lett.* **102** 253504
[12] Tanaka T., Nakano Y, Kasai S 2013 *Jap. J. Appl. Phys.* **52** UNSP 06GE07

[13] Kannan E S, Bisotto I, Portal J-C, Beck T J, Jalabert L 2012 *Appl. Phys. Lett.* **101** 143504

[14] Ganichev S D, Tarasenko S A, Belkov V V, Olbrich P, Eder W, Yakovlev D R, Kolkovsky V, Zaleszczyk W, Karczewski G, Wojtowicz T and Weiss D 2009 *Phys. Rev. Lett.* **102** 156602

[15] Costache M V and Valenzuela S O 2010 Science **330** 6011

[16] Karch J, Tarasenko S A, Ivchenko E L, Kamann J, Olbrich P, Utz M, Kvon Z D and Ganichev S D 2011 *Phys. Rev. B* **83** 121312

[17] Jiang Y, Low T, Chang K, Katsnelson M I and Guinea F 2013 *Phys. Rev. Lett.* **110** 046601

[18] Drexler C, Tarasenko S A, Olbrich P, Karch J, Hirmer M, Müller F, Gmitra M, Fabian J, Yakimova R, Lara-Avila S, Kubatkin S, Wang M, Vajtai R, Ajayan P M, Kono J and Ganichev S D 2013 *Nature Nanotechn.* **8** 104

[19] Fal'ko V I 1989 *Fiz. Tvedr. Tela* **31** 29
Fal'ko V I 1989 *Sov. Phys. Solid State* **31** 561 (Engl. Transl.)

[20] Tarasenko S A 2011 *Phys. Rev. B* **83** 035313

[21] Ando T, Fowler A, and Stern F 1982 *Rev. Mod. Phys.* **54** 437

[22] Ganichev S D, Yassievich I N and Prettl W 2002 *J. Phys.: Condens. Matter* **14** R1263

[23] Karch J, Olbrich P, Schmalzbauer M, Zoth M, Brinsteiner C, Fehrenbacher M, Wurstbauer U, Glazov M M, Tarasenko S A, Ivchenko E L, Weiss D, Eroms J, Yakimova R, Lara-Avila S, Kubatkin S and Ganichev S D 2010 *Phys. Rev. Lett.* **105** 227402

[24] Ganichev S D, Terent'ev Ya V and Yaroshetskii I D 1985 *Pisma Zh. Tekh. Fiz.* **11** 46
Ganichev S D, Terent'ev Ya V and Yaroshetskii I D 1985 *Sov. Tech. Phys. Lett.* **11** 20 (Engl. Transl.)

[25] E. Ziemann E, Ganichev S D, Yassievich I N, Perel V I, *et al.*, Prettl W 2000 *J. Appl. Phys.* **87** 3843

[26] Ganichev S D, Ivchenko E L and Prettl W 2002 *Physica E* **14** 166

[27] Karch J, Tarasenko S A, Olbrich P, Schönberger T, Reitmaier C, Plohmann D, Kvon Z D and Ganichev S D 2010 *J. Phys.: Condens. Matter* **22** 355307

[28] Dyakonov M I and Shur M S 1996 *IEEE Trans. Electron Devices* **43** 380

[29] Schuster F, Coquillat D, Videlier H, Sakowicz M, Teppe F, Dussopt L, Giffard B, Skotnicki Th and Knap W 2011 *Optics Express* **19** 7827

[30] Drexler C, Dyakonova N, Olbrich P, Karch J, Schafberger M, Karpierz K, Mityagin Yu, Lifshits M B, Teppe F, Klimenko O, Meziani Y M, Knap W and Ganichev S D 2012 *J. Appl. Phys.* **111** 124504

[31] Kibis O V 1999 *Zh. Eksp. Teor. Fiz.* **115** 959
Kibis O V 1999 *JETP* **88** 527 (Engl. Transl.)

[32] Tarasenko S A 2008 *Phys. Rev. B* **77** 085328